AEROELASTIC SIMULATION OF THE TAIL SHAKE PHENOMENON

Ulrich Schäferlein, Manuel Keßler and Ewald Krämer

Institute of Aerodynamics and Gas Dynamics (IAG), University of Stuttgart
Pfaffenwaldring 21, Stuttgart, 70569, Germany
schaeferlein@iag.uni-stuttgart.de

Abstract

Rotor-fuselage interactions continue to pose a challenge during the design phase of a new helicopter. Quite often, the prototype phase is faced with problems in fast-forward flight caused by strong interactions at the tail, the so-called tail shake phenomenon. The wake of the main rotor, the rotor hub and the airframe impinges on the tail boom causing an excitation of low-frequency eigenmodes of the entire helicopter airframe. The resulting vibrations reduce flight comfort and flight stability in some critical cases. Previous approaches to solve the problem were restricted to wind tunnel tests due to the lack of predictability in terms of numerical methods. A high-fidelity simulation presented in this study by means of a time-resolved coupling between the flow and structural behavior of the helicopter shows significant progress in the prediction potential of the investigated phenomenon. Utilizing higher order methods for the CFD simulation, tightly coupled with a modal-based CSD simulation of the airframe, very good agreement with flight test data of the relevant low-frequency eigenmodes could be achieved.

1 NOMENCLATURE

$1/rev$	once per main rotor revolution
$a_{X/Y/Z}$	acceleration in respective spatial direction
BPF	blade passing frequency
c_{blade}	blade chord length
c_p	pressure coefficient
CFD	Computational Fluid Dynamics
CSD	Computational Structure Dynamics
DoF	degrees of freedom
$F_{X/Y/Z}$	force in respective spatial direction
MGB	main gearbox
t	time
$v_{X/Y/Z}$	velocity in respective spatial direction
WENO	Weighted Essentially Non-Oscillatory Scheme
ω	eigen-frequency
ζ	modal damping coefficient

2 INTRODUCTION

Rotor-fuselage interaction effects are among the most complex topics in the aerodynamic investigation of a helicopter. Such phenomena describe a significant interaction of the rotor wake with structures of the airframe leading to flight instability and reduction in ride comfort. For these interaction phenomena three distinctive flight conditions are important, namely hover, slow-forward flight, and fast-forward flight. In slow-forward flight the so-called pitch-up phenomenon occurs during a flare maneuver for landing, or in transition from hover to forward flight. Due to the interaction of the rotor downwash with the horizontal stabilizer during the maneuver, an abrupt change of thrust causes strong fluctuations of the pitching moment of the helicopter and thus attitude or exceeding mast moments.

However, the focus of the present investigation is the interaction in fast-forward flight, the tail shake phenomenon. This manifests itself in fast-forward flight, with sometimes slight climb or descent rate[1], by strong lateral vibrations, which can seriously affect the performance of the crew[2]. The phenomenon occurs especially at conventional helicopter configurations with single main rotor and is a result of the interaction of turbulent rotor and fuselage wake with the rear structure of the airframe (cf. Figure 1). Various

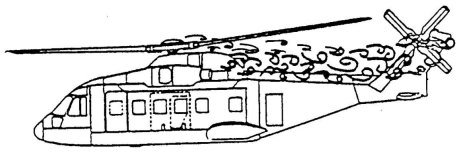

Fig. 1: Schematic illustration of the tail shake phenomenon by[2]

factors such as the rotor hub fairing, engine exhaust and cowling, and the shape, position and dynamics of the tail boom play a key role in the characteristic of the phenomenon. Depending on these factors, interaction between rotor and tail boom can stimulate natural low-frequency modes of the helicopter fuselage

in adverse flight conditions. These vibrations typically occur between one and two times the rotor's rotational frequency[2] and are thus in a frequency range perceived as very unpleasant for humans[3]. When using the helicopter for rescue and patient transport missions, the demand for a low-vibration flight is further increased.

Moreover, tail shake is described as a highly unsteady phenomenon with stochastic character. De Waard and Trouve[2] describe the vibrations as stochastic lateral "kicks" and Strehlow et al.[1] describe them as "bumps" due to a beat of two vibrations. Due to the lack of reliable information before first flight so far, several helicopter designs suffered from strong rotor-fuselage interaction problems during prototype stage, as it has been documented for the EH-101[4], SA365N[5], Tiger[6], CH-53E, UH-60A, S-76[7], AH-64D Longbow Apache[8], NH-90[9], BK-117[10], and EC-135[11]. In some of the cases mentioned, the initial tail boom had to be redesigned because strong rotor-fuselage interactions arose in first flight tests. This negative flight characteristic of the helicopter was usually remedied by a redesign of the tail boom, fairings, or hub cap in shape and position. In some cases, an installation of a hub cap or engine cowling and thus a deflection of the rotor wake enabled some increase of the pressure in the aft wake to stabilize the highly turbulent flow. In case of the EH-101, which already had a hub cap, drag reduction of the upper fuselage fairing reduced the vibration to an acceptable level[4]. Despite the great wealth of experience in helicopter design, the occurrence shows the uncertainties and missing knowledge about the root causes and defining parameters of this phenomenon. In all cases, extensive wind tunnel test campaigns had been conducted to reduce the effects of this problem. The recurring occurrence of prototypes suffering from tail shake proves the high demand on early prediction methods for de-risking. Since wind tunnel test campaigns are connected with high costs and may suffer from reliability problems due to missing rotors and/ or dynamics scaling of the airframe, numerical simulations have become innovative and cost-efficient methods for flow investigations recently.

In the field of numerical methods, some attempts have been undertaken to resolve the rotor-fuselage interaction. However, several investigations noted that a time resolved highly accurate solution of the flow field including all geometric components is required to sufficiently represent the flow characteristics[12]. This restricts this simulation task to the application of highly accurate computational fluid dynamics (CFD) codes. Besides the aerodynamic flow field, the elasticity of the tail boom results in an interaction with the flow field and an impulse exchange between flow and structure. With the enhancement of the DLR CFD code FLOWer by IAG, a mandatory step towards the simulation capabilities of the rotor-fuselage interaction has been made. Different innovative extensions such as more efficient parallelization, deformation routines and the implementation of higher order methods improved the framework for the simulation of helicopter flows[13;14;15;16;17]. In addition, this paper presents the implementation of a time-resolved CFD-CSD coupling feature to enable an efficient consideration of the dynamics of complex CSD structures. This extension makes the holistic representation of the interaction character of the phenomenon possible. Resonance magnifications, aerodynamic damping, and changes in aerodynamic loads can be resolved. This feature enhances the CFD-CSD simulation capabilities towards the simulation of aerodynamically induced tail boom oscillations. A somewhat related approach has been presented recently by Reveles et al.[18]. However, the focus was set on rotor induced vibrations with a low-fidelity non-viscous CFD simulation.

3 SIMULATION FRAMEWORK

Flight state and flight test data

The basis of the investigation is the light medium, twin-engine research helicopter Bluecopter^{TM} from Airbus Helicopters. The demonstrator was developed to prove the feasibility of future eco-friendly helicopter concepts and to demonstrate green technologies in-flight[19]. An extensive flight testing campaign provides, besides demonstration of the future-oriented technology, the basis for the validation of numerical methods. Even if no major rotor-fuselage interaction issues occurred in the flight test, a flight state with stronger induced vibrations could be determined. The examined flight state is a fast-forward flight with slight descent, denoted as TOP36. The flight condition is characterized by a low thrust requirement and, thus, low anti-torque compensation. The low induced velocity of the main rotor as well as the additional descent rate leads to a strong interaction between main rotor wake and tail boom. The airframe orientation is in a slight nose down position with almost zero sideslip and bank angle.

Fig. 2: Light medium, twin-engine research helicopter Bluecopter^{TM} from Airbus Helicopters

Several acceleration and pressure sensors on the airframe provide an extensive database for the validation of the numerical solution.

CFD solver

For the current investigation, the block structured finite volume Reynolds-averaged Navier-Stokes (RANS) CFD code FLOWer of the German Aerospace Center (DLR)[20] is used. The RANS equations are closed using the Wilcox k-ω turbulence model[21]. The time evolution is achieved by integrating the governing differential equation in space with the implicit dual time-stepping approach according to Jameson[22]. In the course of research in the field of helicopter aerodynamics, the CFD solver was extended inhouse with different variants of fifth order spatial WENO schemes[14]. The aim is to guarantee a detailed conservation of the flow field and especially the vortices. Some applications of the implementation to helicopter flows prove the clear advantage of an improved conservation of the vortex structure[23;24;25;26].

For the present simulation, a fifth order WENO-Z scheme according to Borges[27] is applied for the fluid state reconstruction at the cell boundaries. The resulting Riemann problem is solved using the upwind HLLC scheme according to Toro[28].
For an accurate reproduction of the flight state, the main rotor's dynamics are considered by a periodic fluid-structure coupling between the CSD code CAMRAD II[29] and FLOWer. In addition, CAMRAD II allows a 6-DoF trim by adjusting the fuselage orientation, collective and cyclic pitch angles to meet a load free flight state. DoFs may be restricted by setting them to known values and providing specific load objectives.

A detailed modeling of the engine exhaust by prescribing the mass flow's temperature, velocity and swirl allows the consideration of it's influence on the rotor-fuselage interaction. For conservativeness, the engine inlet mass flow is automatically adjusted to the engine exhaust mass flow.

CFD model

Table 1 sums the 62 grid components of the complete helicopter configuration. Extensive blocking of the structured grids allows an efficient parallelization of the simulation, by providing working packages distributed over the computation processes. The body grids are extruded for about 0.5 main rotor blade chord length c_{blade}. At their boundaries, the flow solution is transferred to the off-body grid using the Chimera overset grid technique. The automatically

Component	No. of blocks	No. of cells (mio)
Off-body	25421	346.5
Main rotor blade	5× 384	5× 7.5
Rotor hub system	290	5.3
Fuselage	320	26.7
Engine	2× 724	2× 12.7
Fenestron	3352	43.5.9
Total	**32751**	**484.9**

Table 1: Grid components of complete helicopter CFD setup

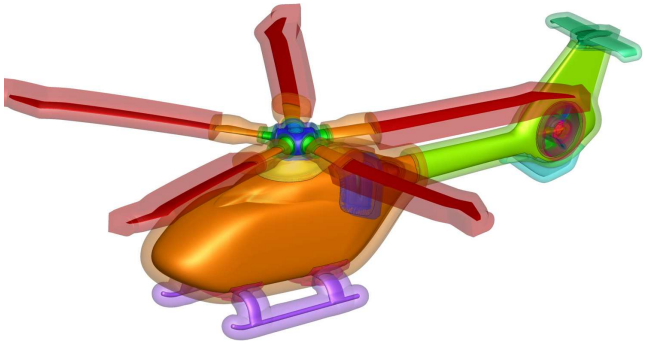

Fig. 3: Helicopter surface geometry and body grids for the CFD simulation

generated Cartesian off-body grid ensures low dissipative transport of the vortex structures. The use of hanging grid nodes allows a tailored adaptation of the spatial resolution. After a periodic flow field is achieved, the tool chain enables an automatic adaptation of the off-body grid to the periodic flow solution. Regions with high flow gradients are identified by the λ_2 value and refined accordingly. In the vicinity of the

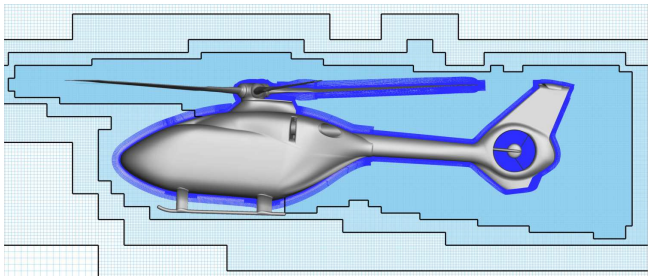

Fig. 4: Overset grid system and off-body resolution levels of the Bluecopter setup

rotor hub, an off-body grid resolution of 0.015 c_{blade} is prescribed. In the rotor disc area and in the rotor hub's wake convection path towards the tail boom, a grid resolution of 0.03 c_{blade} is ensured. If no flow gradient demands for grid refinement of the off-body grid in the vicinity of a body grid, the off-body grid's resolution is set to the resolution required for an accurate interpolation at the Chimera overset grid boundary. The body grids resolve the surface of the he-

licopter with less than 0.06 c_{blade} at the airframe and less than 0.03 c_{blade} at the tail boom with stretching ratios less than 20%. The transitions between the individual grid resolution levels in the Cartesian off-body grid are marked as black lines in Figure 4. Due to the flow-adapted refinement of the off-body grid, a highly efficient concentration of the cells can be achieved.

The CFD-CSD simulation is performed on the High Performance Computing Center (HLRS) in Stuttgart on the Cray XC40 Hazelhen system using 24,000 Intel Haswell cores.

CSD solver

To solve the structure's equations of motion in the modal space, the second-order integration method according to Newmark[30] is applied. Structural damping is modeled in the modal space according to the approach $2\zeta\omega_n$ for the natural modes with the respective eigen frequency ω_n. A modal reduction is used to limit the calculation effort of the CSD computation by restricting the degrees of freedom to the relevant low-frequency mode shapes of the structure. This time-resolved CFD-CSD coupling of the helicopter's airframe is realized by linking the CSD functionality as a library to the CFD solver being computed on-line. This approach preserves the computational efficiency of the highly parallelized CFD-CSD computation. A real eigenvalue analysis in NASTRAN provides the modal matrices, which are used as input for the CSD computation. Modes up to a frequency of the second blade passing frequency are taken into account. Connectivity information between the CFD and CSD discretization is generated fully automatically and allows completely independent discretizations. A more detailed description of the linking process gives the subsequent section.

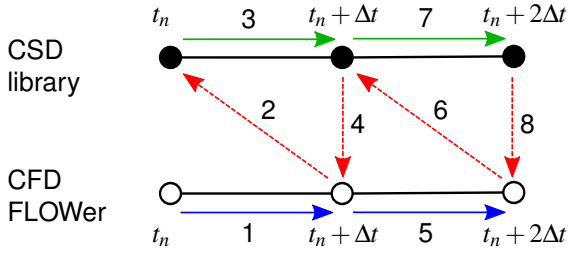

Fig. 5: Time-resolved coupling between CSD library and the CFD code FLOWer using the Gauss-Seidel coupling scheme, also known as serial or "Ping-Pong" algorithm.

Figure 5 shows the time-resolved coupling process between the CFD codes FLOWer and the CSD library linked to FLOWer. A Gauss-Seidel algorithm is applied for the data exchange between the two solvers with the exchange of the data at the end of each time step. Thus, the time integration lags one time step behind the CFD solution. Using a time step of less than 1 ° main rotor azimuth and mode shapes considered up to a frequency of 1.5 BPF, this results in a negligible phase error of less than 8 °. In the relevant low-frequency modes in the range of the rotor rotational frequency, this error is below 1 °. For this reason, the use of other coupling algorithms, such as Jacobi coupling with a concurrent execution of the codes, has been dispensed with.

A fundamental requirement of a CSD-CFD coupling algorithm is the resolution of interaction phenomena with mutual influence. A widely used validation of a fluid-structure coupling tool is the consideration of the phenomenon of singing wires or aeolian tones[31]. Therefore, a cylinder is exposed to a free cross-flow and coupled to a one DoF spring-mass model. At lower Reynolds numbers, a well-defined von Kármán vortex street is formed, which results in a defined load fluctuation on the cylinder surface. If this excitation frequency is close to the natural frequency of the system, an interaction occurs. Depending on the stiffness of the cylinder, in the vicinity of the structure's natural frequency the aerodynamic shedding frequency is shifted towards the structure's natural frequency.

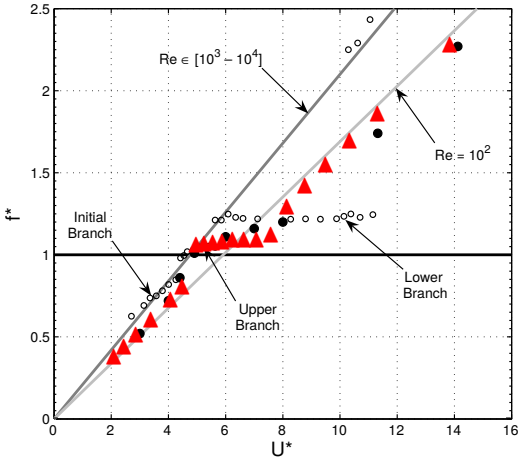

Fig. 6: Reduced frequency response $f^* = f/f_N$ and lock-in zone (illustration adopted from[32]) of an oscillating cylinder in cross-flow. Results from Placzeck et al. (•)[32], Khalak and Williamson (○)[33], and present simulation (▲).

Figure 6 shows the result of a simulation according to Placzek et al.[32], using the presented process chain in comparison with studies from the literature[32;33]. A

very good consistency in the lock-in characteristics is observable. A clear shift of the response frequency f^* towards the natural frequency $f^* = 1.0$ of the cylinder is to be determined. Due to the different stiffness between the examinations, no exact match is to be expected. This validation case demonstrates the ability of the implemented methodology to represent physically correct basic fluid-structure interaction phenomena.

For the present helicopter investigation, the assumption is made that the movements of the rotor hub are marginal and therefore negligible in the CFD. This allows deformation of the cell structure around the main rotor. The assumption thus suppresses movements estimated at less than 1 mm. Due to the movement of the tail rotor, precession effects may be considered. These are estimated on the basis of the axis movement of the tail rotor in the examined flight case and are determined to result in loads, which are two orders of magnitude smaller than the aerodynamically acting loads. Thus, precession effects are neglected as well.
The trimming to a steady flight condition of the helicopter defined by zero translational and angular acceleration is determined by means of the average loads. Load fluctuations around the mean value cause a rigid body movement of the helicopter and thus an acceleration of the airframe. Taking into account the inertia of the helicopter, these accelerations are enforced on the CSD model. Their effect, however, is an order of magnitude below the aerodynamically caused deformations. Due to the linearised representation of the structural model, only small rigid-body accelerations are permitted, which, however, is in agreement with the helicopter's behaviour in the considered flight state.

CSD model

A structural model of the helicopter's airframe was made available by Airbus Helicopters. It is generated in NASTRAN (see Figure 7) and consists of 145,912 nodes with a concentration of the nodes in the region of the tail boom. Based on shake tests of comparable airframe structures, the range of variation of the structural damping is $\zeta = 0.02 - 0.08$. Consequently, a structural damping of $\zeta = 0.04$ is applied for the coupled simulation.

The NASTRAN model does not include rotating structures and describes a simplified load path between the main rotor and the fuselage as well as the tail rotor and tail boom. Doors and rotor mast fairing are not included in the model. The model has been reused from simple structural mechanics simulations and contains therefore partially simplifications and neglects in the fuselage, which are of minor influence to

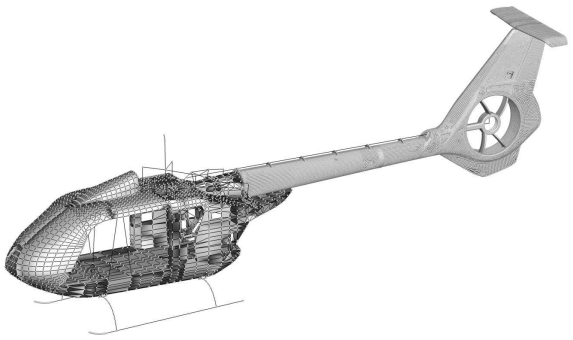

Fig. 7: NASTRAN model of the helicopter's airframe

the tail shake investigation.
A linear eigenvalue analysis of the NASTRAN model provides the mode shapes of the airframe. A modal reduction limits the consideration of the natural-frequencies up to a maximum of 8/rev, which corresponds to 40 natural modes. For higher frequencies the CSD model quality decreases, why this limitation is applied. The considered modes include low-frequency vertical and horizontal bending modes in the vicinity of 1/rev (cf. Figure 9), as well as torsion modes of the tail boom around the 2/rev frequency. In addition, the second and third bending and torsion natural mode are taken into account. The natural modes of the horizontal stabilizer are located around 4/rev and are expressed by tilting movements around the mounting to the fin as well as bending movements of itself.

Figure 8 shows the location of the different mode shapes in the frequency spectrum. In literature, it is

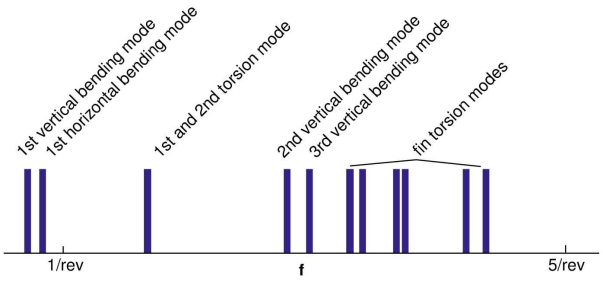

Fig. 8: Considered natural modes of the airframe structure up to 6/rev

assumed that the nature of tail shake is the excitation of the low-frequency eigenmodes in the range of the 1/rev frequency. In the structural model used in this investigation, this means in particular the excitation of the first vertical and horizontal bending modes, as well as a small proportion of the torsion modes. However, due to a torsional share in the horizontal bending mode, any horizontal force influences lateral and torsional deflection. Modes with a higher natural frequency influence this frequency range in negligible amplitudes due to their higher damping.

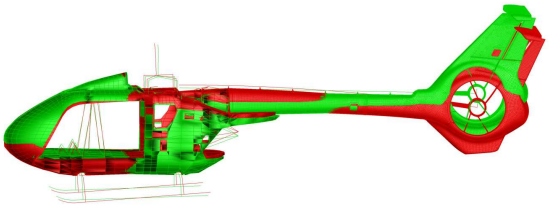

(a) 1st vertical bending mode

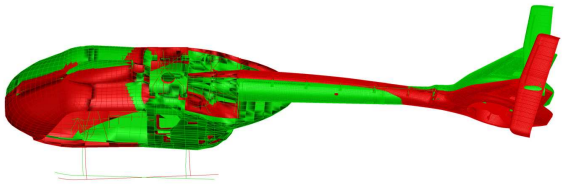

(b) 1st horizontal bending mode

Fig. 9: Tail shake relevant natural mode shapes of the airframe structure

Key aspect of the CFD-CSD coupling is the linking of the CFD and CSD model, which is performed fully automatically during pre-processing in case of the presented coupling framework. For this, the CSD and CFD discretization, which may consist of several individual grids, are provided to the script. In the first step, the distance between the CFD surface node and each CSD node is used to determine the surface nodes of the CSD model (Fig. 10 a)). At these CSD nodes, CFD surface loads are applied and the corresponding displacement is returned to the CFD for grid deformation. Since there may be slight differences between the CSD and CFD model, a tolerance of 0.04 m is used to identify the surface nodes. Due to the resolution of $<$0.02 m of the CFD surface, minor discretization errors are anticipated. In the next step, the nearest CFD cells to the identified CSD surface nodes are marked and the CSD node identifier is noted. The CSD destination node for all other CFD cells is determined via the smallest run length along the CFD surface to the next CFD cell already assigned to a CSD node. Figure 10 b) shows the resulting distances between the CFD cell and CSD nodes. In the area of the doors as well as tailgate, this approach results in large run lengths due to the lack of discretization in the CSD model, which was originally not created for a tail shake analysis. This is, however, a quite plausible assumption by the physical distribution of the loads acting on the doors on their support points on the airframe. A similar picture emerges for the mast and turbine cowling, which are not included in the CSD model as well. A direct assignment of the loads acting on the cowling to the main gearbox nodes of the CSD model would be wrong. Load transfer is applied under consideration of the resulting lever arm.

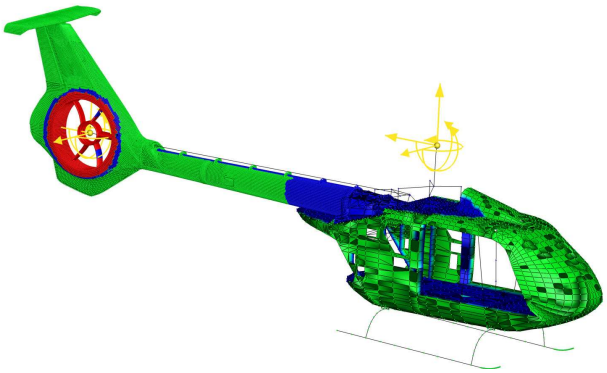

(a) CSD model with identified surface nodes (green), inner nodes (blue), Fenestron duct (red), and external loads (yellow).

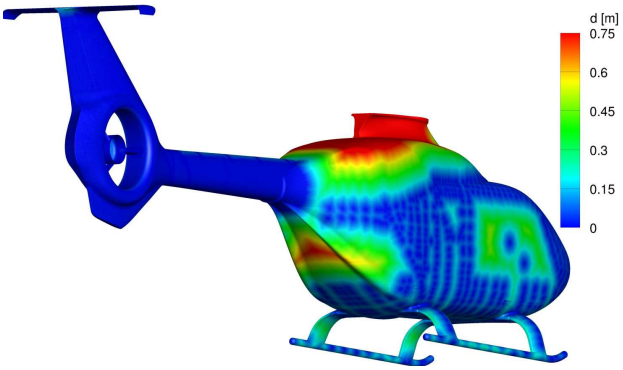

(b) Distance between CFD surface cell and target CSD node

Fig. 10: Linkage between CFD and CSD model

An area around the Fenestron is defined, where no grid deformation is applied (Fig. 10 a) red area) to prevent complications between elastic (Fenestron duct) and non-elastic meshes (Fenestron hub and blades) of the CFD calculation. Therefore, the still elastic CSD region returns only a rigid body movement representing the movement of this section. A narrow band between the rigid and elastic area ensures a smooth interpolation between deformed and rigid body moved CFD grids. Since the area around the Fenestron is very stiff anyway, this assumption is feasible with deviations of less than 1e-5 m between CSD and CFD surface displacement. However, a boundary layer resolution of 1e-6 m makes this method necessary. The translatory and rotatory rigid body movement is defined by the displacement and rotation of the CSD node at the Fenestron hub.

In order to take account of external loads of the main and tail rotor in the calculation of the airframe elasticity, collocation points for these loads are defined in the CSD model (yellow points in Figure 10 a)).

By means of this assignment, no requirements for

e.g. closed / wetted surfaces are introduced and an automation with plausible linking of the two independent discretizations is ensured.

Flight mechanic trim

For the flight mechanical trim of the helicopter towards a steady flight state, a periodic coupling with FLOWer-CAMRAD II is carried out. For this purpose, the airframe orientation angles of the flight test are prescribed, resulting in four remaining degrees of freedom for main rotor and tail rotor control angles. The main rotor thrust, as well as roll and pitch moment, are chosen as trim objectives. The tail rotor collective is adapted to compensate the yaw moment at the helicopter. During the flight mechanic trim, the time-resolved CFD-CSD coupling of the airframe is performed with a aperiodic damping of $\zeta = 1.0$ to suppress airframe oscillations. This makes it possible to take into account the mean influence of the elastic airframe on the trim due to, for example, changed angles of attack on the fin and the horizontal stabilizer. The aperiodic damping assures a fast tracking of the airframe deformation when the rotor wake changes. After completion of the trim, the structure damping is changed to the nominal damping of the model.

Trim convergence is achieved after six trim iterations with a residual of the control angles between the iterations less than 0.05 °. Table 2 shows the comparison with the flight test data. Deviations of less than 0.5 ° for the main rotor control angles show excellent results. The deviation for the tail rotor collective results from the flight-mechanically problematic flight state. Due to the low main rotor thrust and the resulting low torque in combination with the large fin of the helicopter, a reversed tail rotor thrust near zero is required. This flight state shows strong fluctuations in the tail rotor collective during trim with a similar deviation as in previous investigations[34].

DoF	$\Delta_{CFD-exp}[^\circ]$	RMS of exp.
$\Theta_{0,MR}$	-0.15	–
$\Theta_{1s,MR}$	-0.47	0.3
$\Theta_{1c,MR}$	0.20	0.2
$\Theta_{0,TR}$	-5.21	–

Table 2: Control angles after a converged 4-DoF trim compared to the flight test control angles (TOP36)

Transient response and evaluation sequence

After trim convergence is achieved, the structural damping of the airframe is reduced from aperiodic damping to nominal damping. Figure 11 shows a transient response of the airframe's first two eigen modes in terms of their modal displacement. Within section 1

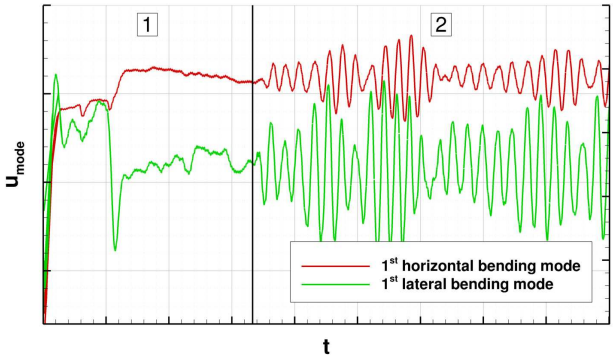

Fig. 11: Transient behavior of the first two airframe's mode shapes' displacement. Section 1: flight mechanic trim with aperiodic damping $\zeta = 1.0$. Section 2: nominal damping.

the flight mechanic trim with an aperiodic damping is performed. The high damping ensures a fast tracking of the airframe response to load changes due to trim corrections. After the trim and a reduction to the nominal damping, a transient oscillation is notable at the beginning of section 2. Subsequently, there is a vibration behavior with approximately the same amplitude level. Due to the broad spectrum in the aerodynamic flow field as well as in the structural dynamics model, there is no clear periodicity over the calculated period. For this behavior with no distinct period over several rotor revolutions, the necessity of a time-resolved coupling, and a long evaluation window without periodic assumption, is inferred. This behavior can also be found in the flight test data, which does not reflect a clear periodicity of the structural mechanics, over a period of 120 s, taking into account the usual fluctuations in flight.

A time window of 3 s (approximately 18 rotor revolutions) is taken for the comparison of the simulation results with the flight test data. In order to ensure comparability with the flight test data, this is divided into 3 s time windows and, in addition to the total average, the fluctuation range of the individual sequences around the average is determined.

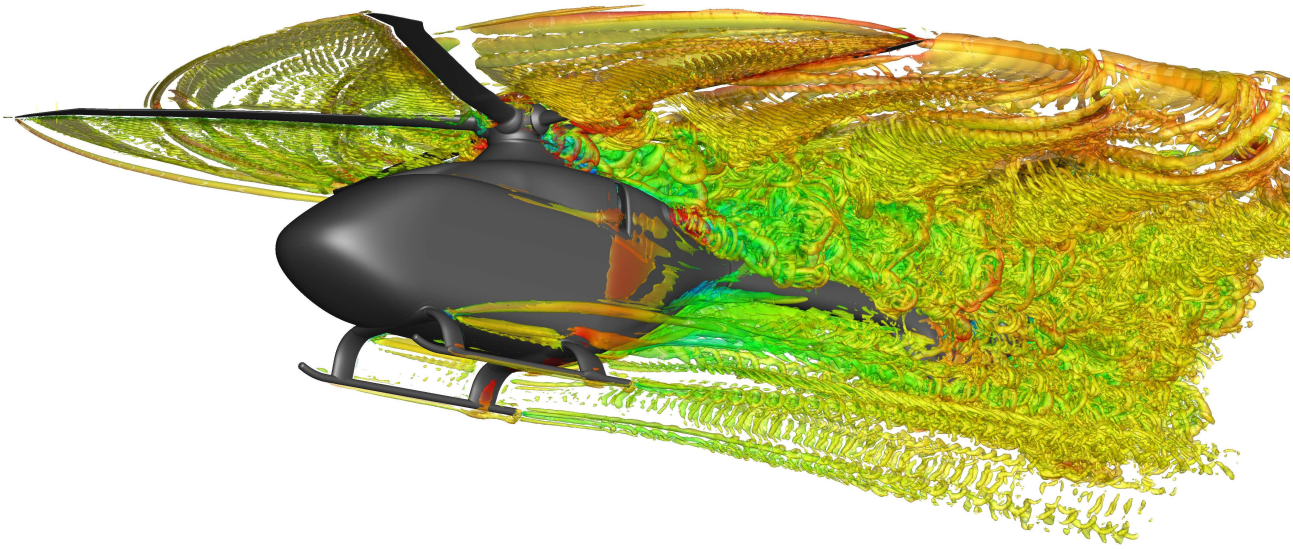

Fig. 12: λ_2-visualization of the flow field around the Bluecopter^{TM} in fast forward - slight descent flight coloured with the local velocity.

4 FLOW FIELD

The flow field around the helicopter shown in Figure 12 illustrates the advantages of the high-fidelity simulation. By means of high spatial and temporal resolution, as well as the application of the higher order method, a detailed conservation, convection, and interaction of the wake structure with the tail boom can be achieved. The influence of the engine exhaust is notably resolved with its temperature and swirl affected flow. The wake of the rotor hub and engine cowling is observable by the high vorticity and lower velocity magnitude. In the wake of the tailgate, a small detachment region is formed with only weak turbulence. Strakes on the outer shell, proposed by drag optimizations[35], ensure discrete vortex strands in the wake of the fuselage and thus a stable and defined structure. Aerodynamic lining of the landing gear struts cause considerably less turbulence induced into the flow field compared to cylindrically shaped struts. The detachment at the rear edge of the landing gear forms typical wake structures with von Kármán-like detachment characteristics.

4.1 Wake structure analysis

To analyse the interactions at the tail boom with individual airframe components' wake, an investigation is carried out using massless particles. For this purpose, every 5° main rotor azimuth the particles are seeded on the respective surface section into the flow and convected two rotor revolutions on the basis of the aerodynamic flow solution. Figure 13 shows the particle positions after two main rotor revolutions coloured with its respective source. The convection of the rotor head wake (blue), upper fairing (red), and engine (yellow) show a strong mixing without a clear demarcation of the individual shares. In case of the skids (green) the main wake path forms the previously noticed von Kármán-like paths, with sheared convecting towards the tail boom. However, no significant influence on the horizontal stabilizer is observed in this flight state when considering the particle positions of the components.

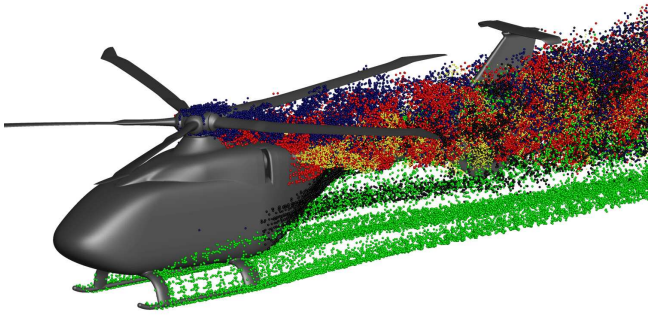

Fig. 13: Visualization of the wake paths of the individual geometric components

A more detailed breakdown of the wake influence to the tail boom's surface gives Figure 14. Over a time window of two rotor revolutions, the kinetic energy of the particles closely convecting past the surface is summed. The dyed areas on the airframe surface show the wake's influence with strong influence

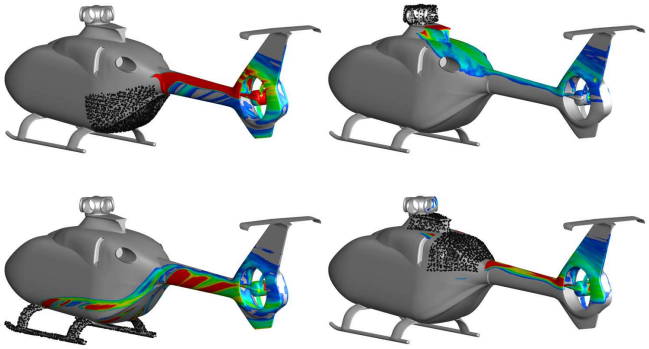

Fig. 14: Wake interaction areas of different airframe components. Top left: rear door, top right: rotor hub, bottom left: skids, bottom right: engine and rotor mast cowling.

marked in red and weak in blue. The illustrated interaction of the fuselage tailgate (upper left) shows a clear interaction of the wake with the tail boom on the upper half of the Fenestron. It is quite concentrated without a strong spread on this area. In the case of the rotor hub wake (upper right), a slightly different interaction occurs. It impinges more on the fin of the tail boom and is spread over a larger area. The skids' wake (lower left), which primarily convects below the tail boom, nevertheless shows an upward trend with interactions on the underside of the tail boom due to the fuselage trailing vortices. Thus, the illustrated interaction intensity of the skids' wake is distorted due to the energy entry by the rear door's wake. The upper fairing (lower right) shows a concentrated effect on the tail boom in the upper half of the Fenestron as well as on the transition to the fin. However, all individual components' influence is mainly concentrated in the area above the Fenestron rotation axis and below the horizontal stabilizer.

4.2 Airframe elasticity

Figure 15 a) depicts the mean deflection of the airframe CFD surface over the evaluation window of 3.5 s. It should be noted that, as expected, negligible deformations occur in the vicinity of the passenger cabin. In the region of the tail boom, however, a clear deflection in the vertical direction can be detected, which deforms the tail boom downward. In addition, slight deviations occur in the horizontal direction, which leads to a slight mean rotation of the rotation axis of the Fenestron of approximately 1.2° forward. The unsteady deformation of the airframe is represented by the root-mean-square value of the deflection around the mean value in Figure 15 b). A logarithmic scaling of the contour gives a good insight into the unsteady deformation of the airframe. Comparable to the mean deflection, strong unsteady behaviour is found at the tail boom. Particularly strong

(a) Mean deflection (red) and rigid airframe (grey)

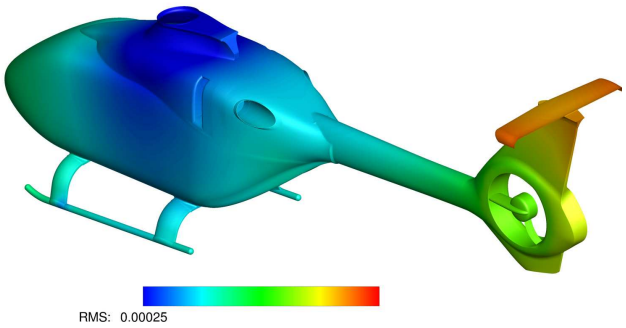

(b) RMS of deflection

Fig. 15: Mean deflection and RMS value of the airframe surface due to aero-elasticity

fluctuations can be detected on the horizontal stabilizer due to the superposition of its bending and tilting modes with those of the tail boom. In the middle sector of the cabin shell, a range with only minimal fluctuation is found, whereas significantly higher deflections are again present in the airframe's nose region. This can be traced back to the excitation of the lateral bending mode, which has a vibration node in this area and contributes decisively to the tail shake behavior of the helicopter[2]. The location of the bending modes' junction point favores the method of a rigid rotor hub assumed on the CFD side.

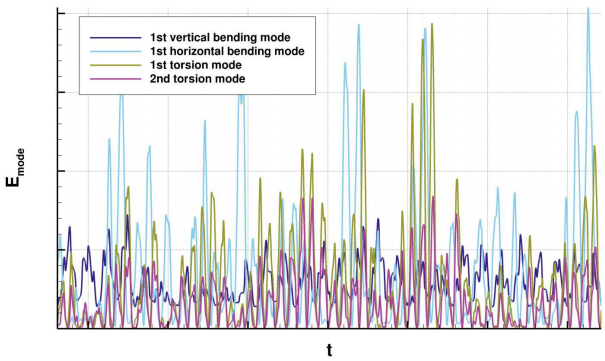

Fig. 16: Overall modal energy of the first four airframe eigenmodes over the evaluation sequence

The excitations of individual mode shapes are shown in Figure 16 on the basis of the variation of the modal energy. For clarity, only the relevant modes in the low-frequency range are shown with decisive excitation. Ideally, there is a constant energy of the mode shape. In this case, however, a strong variation in the mode shapes' energy is recognizable. This results from the continuously fluctuating excitation force in the strongly non-stationary flow field. Comparing the different energy fluctuations, the first horizontal bending mode and torsion modes show a strong variation, whereas the amplitude of first vertical bending is considerably smaller. This results from the previously mentioned strong torsional share of the horizontal bending mode which affects the torsion modes as well. Although no clear periodicity can be detected over a period of three seconds (around 20 rotor revolutions), no significant trend of the time-averaged energy level of each mode is present. Particularly when considering the first horizontal bending mode, a strong recurring energy variation occurs, which indicates a beating. This behavior is similar to that of the crew's classification of tail shake and other papers describing tail shake with a beating character. Since the experimental data also show strong fluctuations without a clearly recurring character, the choice of an evaluation window of three seconds without an assumption of periodicity is the most reasonable approach. This fact underlines the necessity of a time-resolved coupling approach to reproduce the structural dynamics in this flight state.

5 ACCELERATION SENSORS

A comparison of vibration measurements at the tail boom between flight test data and simulation is shown in Figure 17. The ordinate shows the logarithmic sensor's acceleration over frequency spectrum. The mean value (red) of the 3 s time windows of the flight experiment as well as their minimal and maximal fluctuation range (grey, dashed) are shown in the Figure. In the case of the vertical acceleration sensor on the horizontal stabilizer (Fig. 17 a)), there is generally a very good agreement in absolute values as well as the distinctive characteristics of the spectrum. Especially the tail shake relevant low-frequency mode shapes show comparable acceleration values within the variation range of the flight test. Due to the excitation of the first vertical bending mode, the low-frequency range is triggered. At slightly higher frequencies, significantly higher amplitudes are found due to the excitation of the torsion modes of the tail boom. However, these occur in the simulation with a slightly reduced frequency. The most pronounced acceleration is shown at the first blade passing frequency. Both, position and amplitude, are simulated accurately. For the first BPF, light secondary peaks

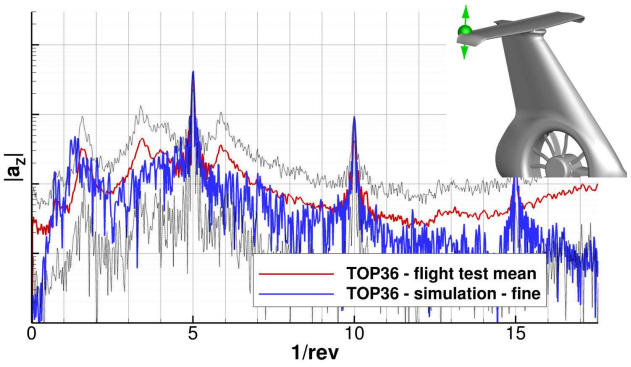

(a) Vertical horizontal stabilizer vibration

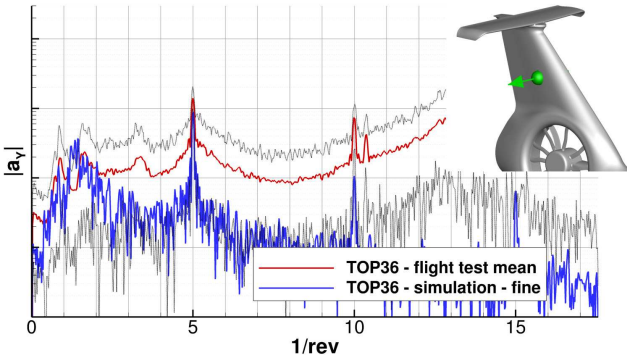

(b) Lateral fin vibration

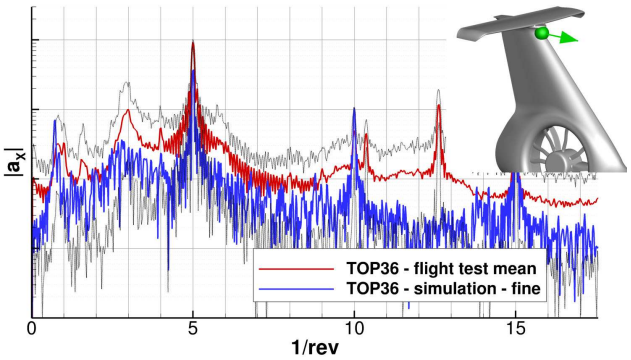

(c) Longitudinal fin vibration

Fig. 17: Frequency spectra of acceleration measurements at the tail boom (grey indicates flight test variation)

also occur in the flight test, which lie in the frequency range of the bending and teetering modes of the horizontal stabilizer. These are not to be found in this simulation. Nevertheless, a similar gradient towards the first BPF is shown. To higher frequencies, a similar curve is found, with a high acceleration amplitude at the second BPF. This is consistent with the previously analyzed flow field due to the convection of the blade tip vortices closely below the horizontal stabilizer. The resulting impulsive load induction results in an excitation of the fundamental BPF and its harmonics. For higher frequencies than the second BPF, there are stronger deviations from the flight test. With the focus on the low-frequency range and the limitation of the

airframe modes considered up to approximately the 2^{nd} BPF, this deviation is of secondary importance.

When analyzing the sensor position at the fin of the tail boom in the lateral direction (Fig. 17 b)), a good correlation of the acceleration values in the low-frequency range can again be found. Accordance with the determinants of the first lateral bending behavior is present. The slightly higher torsion modes, whose movement is in the vertical and horizontal directions, also show the same amplitude as in the flight test with a slightly lower frequency. As with the previous sensor, the amplitude of the first BPFs is in good agreement with the flight test. The second BPF, however, is underestimated by an order of magnitude. In contrast to the sensor of the horizontal stabilizers, the broadband noise between the prominent peaks is clearly below the mean value, but still within the fluctuation range. One possible cause is less stiffness at this location on the real helicopter.
The oscillation of the tail boom in the longitudinal direction is shown in Figure 17 c). The excitation of the vertical bending mode is shown in the low-frequency range. The accelerations due to the torsion modes acting in the other directions are not noticeably pronounced. In the area below the first BPF, a range of higher amplitude is found, which is represented in the trend but slightly underestimated. As in the case of the horizontal stabilizer, there is again an impulsive characteristic of the excitations of the BPFs. Further peaks are to be found between the second and third BPF. These are in the range of the Fenestron rotational frequency and are based on mechanically induced fluctuations, e.g. slight imbalance.

5.1 Main gearbox vibrations

Main gearbox (MGB) sensors are compared in Figure 18. The low frequency mode shapes do agree within the fluctuation range and show good accordance. However, numerous additional frequencies are excited in the flight test data besides the expected frequencies. In the range of the rotor rotational frequency, the flight test data shows an increased peak, which can be traced back to possible mechanical vibrations in the transmission. In the range slightly below the first BPF, a higher broadband level is represented in the flight test as well as in the simulation. For frequencies above the first BPF, an insufficient match of the simulation data is found. This may be due to the coarse discretization of the CSD model in this area. The first BPF itself is represented with a significantly lower amplitude, as well as its harmonics. In this case, an improved modeling of the load path from the rotor hub to the airframe may be necessary. In principle, a comparable tendency of the vibration behavior at the main gearbox is shown, but

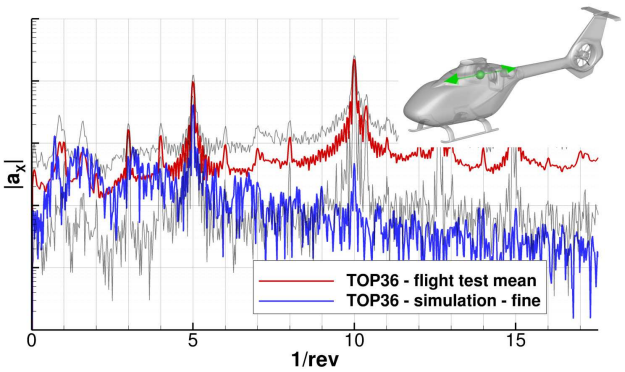

(a) longitudinal MGB vibration

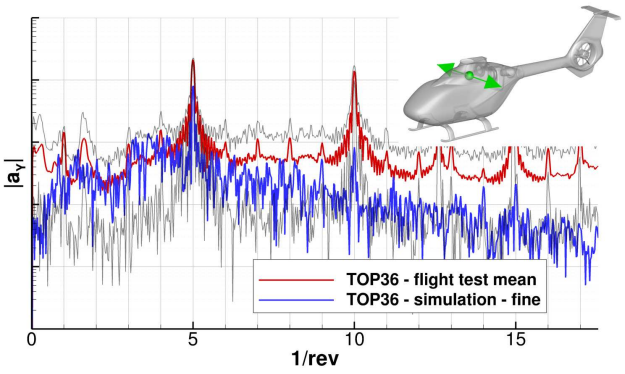

(b) lateral MGB vibration

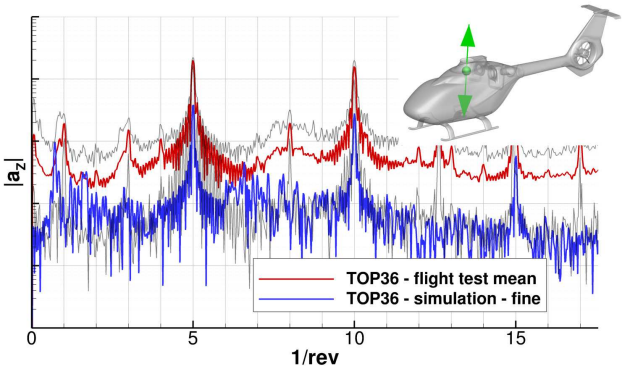

(c) vertical MGB vibration

Fig. 18: Frequency spectra of acceleration measurements at the main gearbox (grey indicates flight test variation)

is of secondary importance for the evaluation of the tail shake behavior of the helicopter. However, with few improvements, this method offers the potential to more precisely resolve the blade harmonics' vibrations in these areas.

6 TAIL BOOM MOMENTS

To determine the overall tail boom load, the moments at the transition to the helicopter cabin are determined by means of strain gauge measurements. Figure 19 shows the frequency spectra of flap, lead-lag and torsion moment at the tail boom root with the mean value

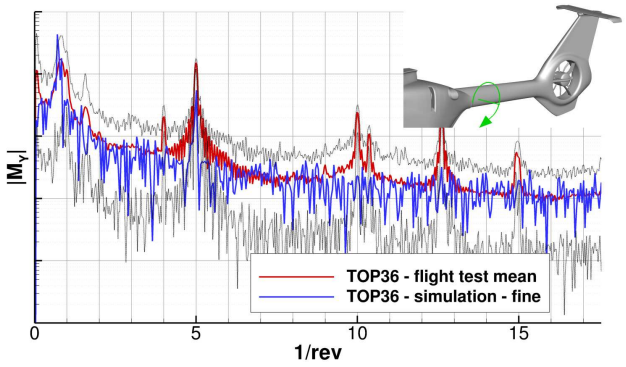

(a) Tail boom flap moment

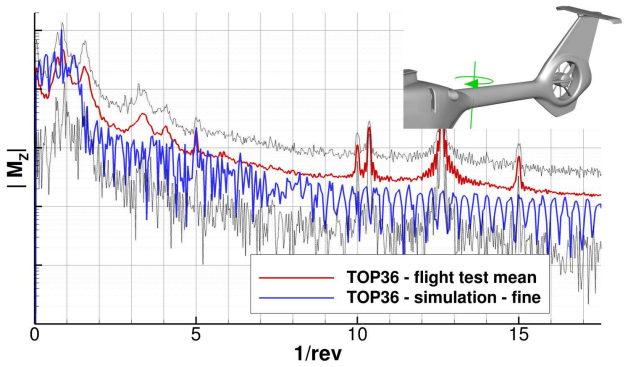

(b) Tail boom lead-lag moment

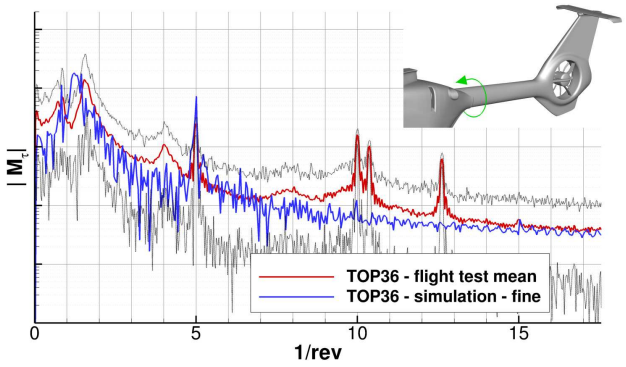

(c) Tail boom torsion moment

Fig. 19: Frequency spectra of bending moment measurements at the tail boom (grey indicates flight test variation)

as well as the variance. In order to perform a comparison with the simulation, the time-resolved deformations of the CSD model are evaluated at this point. By means of a second order central difference-operator in the respective spatial direction, the bending line and thus the locally occurring moment can be determined. Due to missing information on the local stiffness, the moment is scaled to a comparable absolute value to the flight test. The order of magnitude required for this is in a plausible range for the assumed stiffness. Considering the flap moment around the tail boom root (Fig. 19 a)), clear accordance between flight test and simulation exists. In the low-frequency range, the amplitude due to the vertical bending moment is recognizable. For slightly higher frequencies, a minor increase due to the torsion modes is notable. Due to the influence of the blade tip vortices on the horizontal stabilizer lift, there is a considerable variation with the BPF. However, this is slightly lower in the simulation. Harmonics of the BPF do not occur in the simulation, different to the flight test. Nevertheless, in addition to the low-frequency fluctuations, a very good agreement of the gradient of broadband oscillation is shown. In the case of the lead-lag moment (Fig. 19 b)), a similar characteristic is shown, with good consistency of the low-frequency fluctuations. The significantly lower lateral influence of the blade tip vortices is represented by the simulation as in the flight test. Higher-frequency peaks are again measured, which are presumably caused by mechanically induced fluctuations. The torsional moment (Fig. 19 c)) shows a marked amplitude in the range of the torsion modes, which are reproduced in the simulation with a slightly reduced frequency. The spectrum's progression also shows a very good agreement of the gradient towards higher frequencies. Moreover, the peak at the first BPF is in good agreement with the flight test. No BPF harmonics are present in the simulation. In the flight test, mechanically induced fluctuations are again evident. Due to the sensitive nature of this evaluation method, the simulations are very satisfactory. The general characteristic with a good agreement of the tail shake-relevant low-frequency fluctuations is represented by the simulation.

7 PRESSURE SENSORS

A comparison of the frequency spectra of pressure measurements at the fin is shown in Figure 20. Three different vertical positions on the fin are selected. Due to the interaction of the blade tip vortices and the structural deflections, these are of particular interest for the comparison of the simulation data and the measured data. In the case of the sensor at the foot of the fin (cf. Figure 20 a)), slightly above the Fenestron duct, a good agreement is found in the broadband level of the pressure fluctuations. Absolute values as well as the gradient towards higher frequencies are in good agreement. In the simulation, however, pressure fluctuations in the area of the first bending mode and torsion mode can be clearly seen, which are missing in the mean values of the flight test. However, the simulation peaks remain within the fluctuation range on the part of the simulation. Considering the central sensor (cf. Figure 20 b)), a clear formation of the first BPF is present, which results from the closer position of the pressure sensor to the interaction position of the blade tip vortices with the fin. In addition to the higher amplitudes of the low-frequency modes, the simulation's broadband noise level slightly deviates. The reduction correlates with the airframe

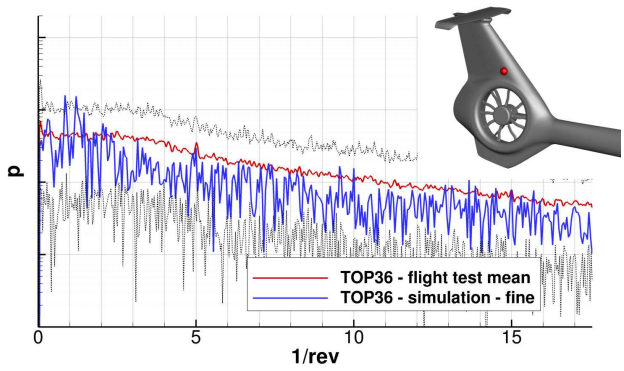

(a) lower location (PFINR1)

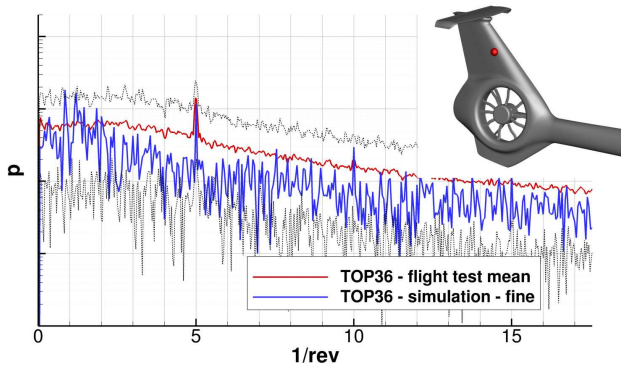

(b) middle location (PFINR2)

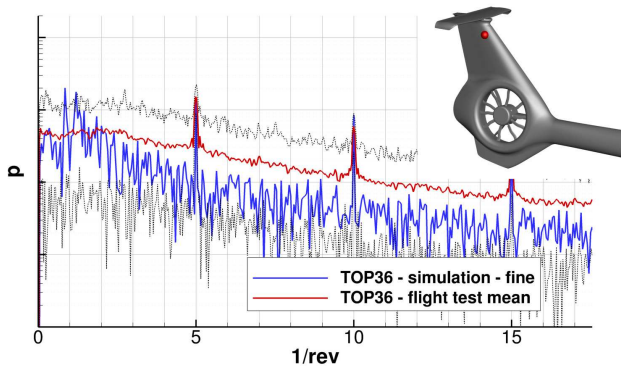

(c) upper location (PFINR3)

Fig. 20: Pressure sensors on the vertical fin of the tail boom (grey indicates flight test variation)

wake analysis shown previously, which reveals an interaction of the wake primarily with the fin's lower region. In the flight test, on the other hand, a nearly unchanged broadband level is observed. The upper sensor of the fin (cf. Figure 20 c)) shows similar characteristics. Due to the close proximity to the blade tip vortices, a strong development of the first BPF and its harmonics occur due to the impulsive characteristic. These are reproduced very well in the simulation, which suggests that the position and strength of the blade tip vortices are very well reproduced. When evaluating broadband noise, the simulation shows a further reduction due to the position further outside the highly turbulent airframe wake. This behavior can not be found in the flight test data on this sensor either. Due to the accurate delineation of the main rotor wake and thus the demarcation of the airframe wake, the missing characteristics in the measured data is unexplainable.

Sensor	Flight test c_p	Simulation c_p
PFINR1	-3.072e-03	-4.163e-03
PFINR2	-6.781e-03	-4.625e-03
PFINR3	-1.540e-02	-1.498e-02

Table 3: c_p values of flight test and simulation of considered pressure sensors

The mean pressure coefficient c_p of simulation and flight test of the considered pressure sensors are compared in Table 3. All sensors reproduce a suction on the sensor locations with a decrease of pressure from the lower towards the upper fin. Absolute c_p values do differ with acceptable differences and the main characteristic is captured by the simulation. Due to the mounting of the sensors on the outside of the helicopter and the resulting thin sockets, which are not included in the CFD simulation, slight deviations are also to be expected. A more detailed comparison assessment would require additional sensors to investigate the load distribution over the fin.

8 POTENTIAL EXCITATION SOURCE

On the basis of numerical simulations, the aim is to gain insight into the mechanisms of action of the phenomenon. Therefore, potential causes for the excitation of the structural vibrations are identified in the following. Due to the weak occurrence of tail shake in the considered helicopter model, a clear identification of a main cause for tail shake is unfortunately not possible. For this reason, sources are investigated, which influence the load fluctuations at the tail boom and thus the structural excitation to a not insignificant extent.

8.1 Energy input of aerodynamic loads

First, the areas on the surface are identified in which the acting aerodynamic loads cause an input or destruction of the mode's energy. For this purpose, the time-resolved loads are multiplied by the sign of the locally occurring modal velocity vector and summed over the evaluation time window. In order to separate the energy entries for the respective modes, the local motion vector and the load input of each mode are considered individually. Figure 21 shows the total load for each mode, which represents an energy input with a positive sign and an energy output with a negative sign. It is to be noted that the structural restoring loads are not taken into account in this visualization.

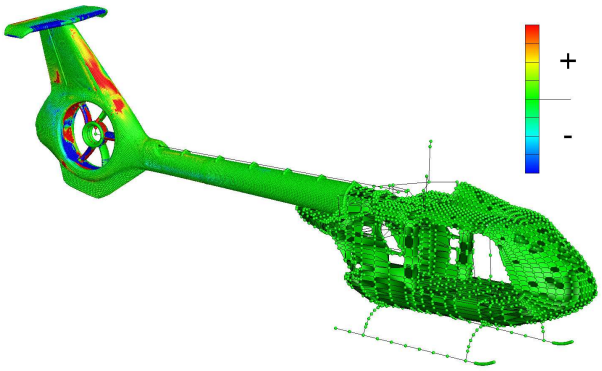

(a) 1st vertical bending mode

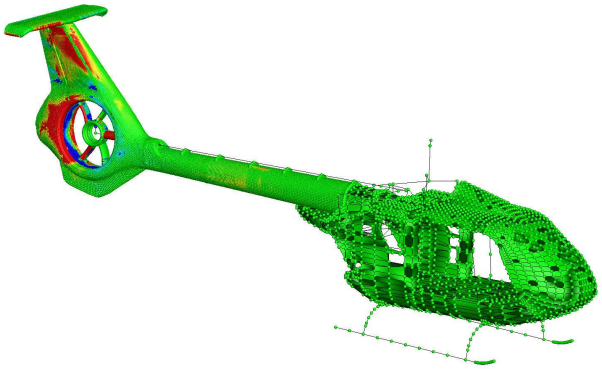

(b) 1st lateral bending mode

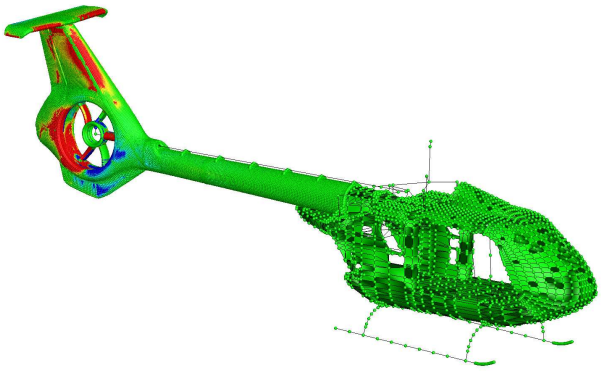

(c) 2nd torsion mode

Fig. 21: Surface areas with loads contributing to mode excitation and damping

Thus, a positive balance of the aerodynamic energies is necessary to excite the respective mode.

When analyzing the 1st vertical bending mode (Figure 21 a)), a significant concentration of the loads' influence on the horizontal stabilizer and the Fenestron duct can be seen. A slightly unbalanced energy between left and right horizontal stabilizer is shown, but with the overall balance of a negative energy input. The backward tilted leading edge of the fin also shows a markable influence on the energy balance with a positive sign. A stronger influence is found in the lower part of the fin, where the interaction with the airframe wake takes places. Within the Fenestron duct, a relevant load fluctuation is to be noted. The change of sign within the duct indicates a fluctuating total load of the Fenestron in the relevant frequency range of the mode shape.

The lateral bending mode (Figure 21 b)) is influenced primarily by the fin and the rear Fenestron duct area. In this case of the fin, a positive energy input of the attacking loads is determined, which indicates a predominant phase shift of less than 90 ° between load and velocity. A same behaviour is found at the Fenestron duct area. High load fluctuations in this area indicate a local suction area due to Fenestron mass throughput. Small energy inputs on the horizontal stabilizer are notable, caused by the torsional proportion of the lateral bending modes, whereby a share of the stabilizers' lift contribute to the energy balance. For the second torsion modes (Figure 21 c)), a similar picture is shown, with strong fluctuations at the tail boom in the fin area.

8.2 Fenestron operation

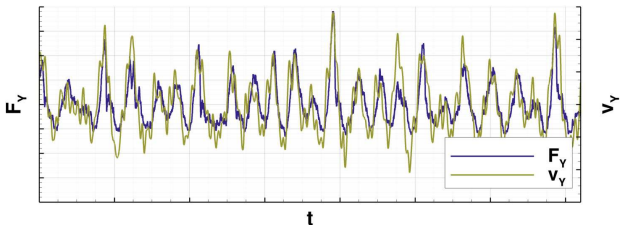

(a) rear Fenestron duct

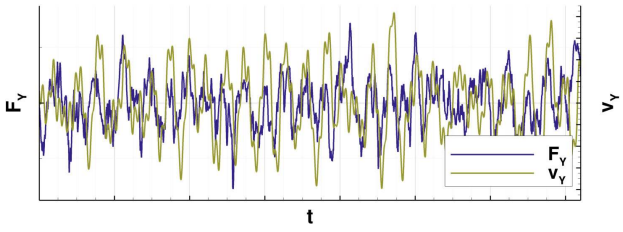

(b) fin

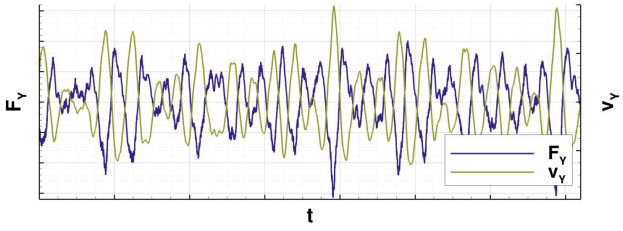

(c) Fenestron hub

Fig. 22: Lateral force and velocity for points at different tail boom locations (random scale)

A time-resolved illustration of local forces and velocities at the tail boom in lateral direction is done in Figure 22. A previously found excitation of the lateral modes in the area of the Fenestron duct and fin can

be clearly seen in Figure 22 a) and b), due to an in-phase fluctuation of speed and force. In the case of the fin, this can not be seen as clearly as in the case of the Fenestron duct, owing to the strong broadband noise of the airframe wake. Contrary to these areas with energy input, the lateral force on the Fenestron hub (cf. Figure 22 c)) has a strong dampening effect on the lateral modes. The load, with phase inverse to the velocity, ensures an energy output. This results in one of the possible problems which will be further discussed. The strongly fluctuating Fenestron load, which has basically a dampening effect, leads in combination with the nearly zero mean load to an inverse flow through the Fenestron. This inverse flow leads to a strong fluctuation at the Fenestron duct, which in turn has a stimulating effect. The time-averaged flow around the Fenestron shows the development of the suction area at the rear Fenestron duct region as well as the reverse flow through the Fenestron. This

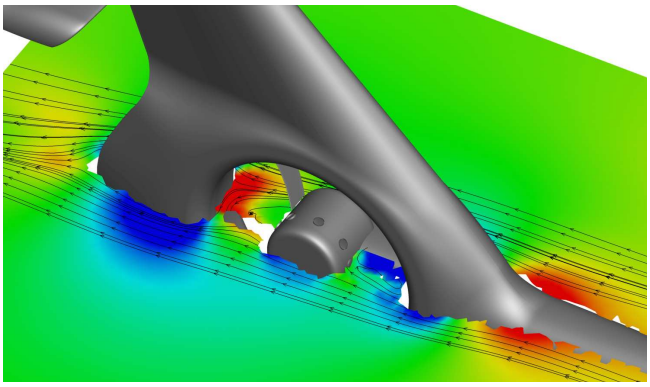

Fig. 23: Time-averaged flow field around the Fenestron

suggests that the operation of the Fenestron near the zero thrust results in a highly unfavorable flow condition, which supports the excitation of the lateral and torsional tail boom mode shapes.

8.3 Airframe wake

Based on two million sensor points in the vicinity of the rotor hub and tail boom, an evaluation of the flow field is carried out over the three second time window. For this purpose, the local λ_2 fluctuation in the frequency range between 0.5/rev and 2/rev is filtered at the sensor points (cf. Figure 24). This can be used to obtain conclusions about possible wake structures in the frequency range relevant for the excitation of low-frequency modes. For visualization purposes, the sensor points are connected to form a volume. On the basis of slices and iso-surface, areas are marked with high fluctuations in the mentioned frequency range.

The area of high spectral intensity is clearly limited to the airframe wake, as well as to the surroundings of

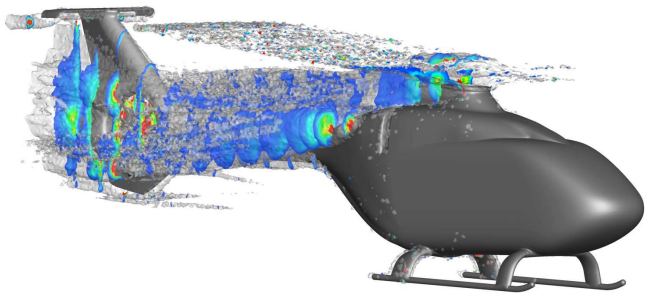

Fig. 24: Regions with high spectral λ_2 energy between 0.5/rev - 2/rev

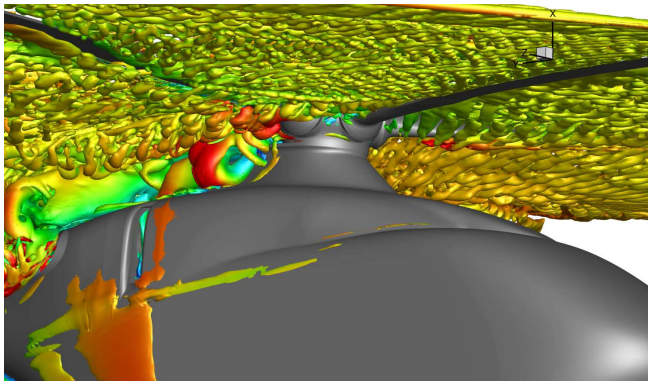

Fig. 25: Instantaneous vortex visualization around the rotor hub

the tail boom. Due to the negligible elastic deformation of the helicopter airframe in the area of the rotor hub, the resulting fluctuations are caused by aerodynamics only. These are induced by detachment phenomena at the rotor hub and blade root, as well as due to interactions between the rotor hub wake and mast fairing. A further contribution is provided by the engine exhaust, which seems to introduce further energy in this spectral range into the wake. The resulting wake decreases in intensity over the convection length towards the tail boom. The higher intensity around the tail boom is due to the elasticity and hence to the fluctuations of the flow around the tail boom. Even if the airframe wake loses intensity due to its interaction with the tail boom, a contribution to the excitation of the low-frequency mode shapes is plausible.

With a λ_2-visualization of the vortex structure (cf. Figure 25), the formation of large-scale vortex structures on the rotor hub and the mast fairing becomes apparent. The transition between the rotating rotor hub and the horizontal outflow of the mast fairing is characterized by a vortex structure. This is presumably formed due to the impingement of detached blade root and attached mast faring flow. For a better resolution of this detachment, the use of an LES simulation could be advantageous for further studies.

8.4 Engine exhaust

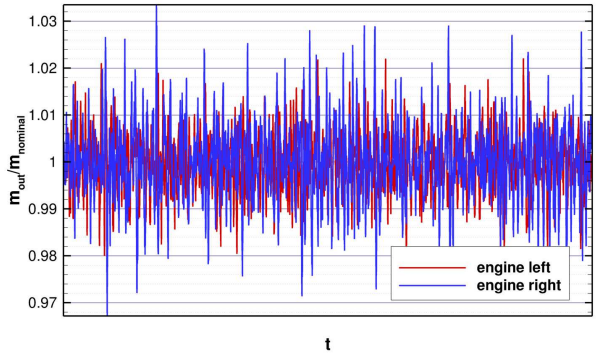

(a) Mass flow through the engines

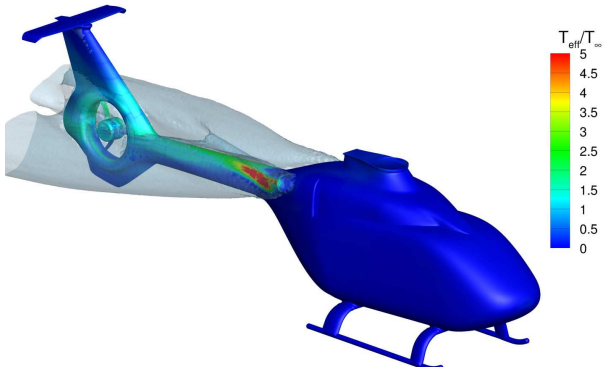

(b) Average engine exhaust convection area and caused temperature fluctuation on the airframe surface

Fig. 26: Operating condition of engine and wake influence

As previously shown a factor for turbulent energy input in the airframe wake is the engine exhaust. In addition to a prescribed mass flow, the swirl of the engine is considered. Due to the low power required in the considered flight state and thus the operation of the engines outside of the design points, a higher swirl in the exhaust is present. Figure 26 a) shows the mass flow through the engines. Due to the fluctuating pressure field at the outlet, slight fluctuations occur around the nominal mass flow, which remain in a range of less than 3 %. Nevertheless, impulsive fluctuations can be seen, which are subsequently introduced into the wake of the airframe. Figure 26 b) shows the mean convection range of the two engine exhausts (isosurface) as well as the temperature fluctuation caused on the surface. Directly at the transition to the tail boom, stronger fluctuations are found, which, however, lose very much in strength and cause only negligible fluctuations in the area of the Fenestron. The convection area shows a clear asymmetry of the wake which correlates with the overall wake of the helicopter. The engine can be an excitation source from these findings, but in the present case no significant influence can be traced back to the engine.

9 ROBUSTNESS OF THE METHOD TO FLIGHT STATE VARIATION

In order to investigate the influence of the flight condition on the application of the fluid-structure coupling method, a further flight state is investigated. This is taken from the same flight test campaign and classified by the crew with a lower tail shake characteristic than flight condition TOP36. The considered flight state, TOP14, is a 140 kn level flight with a side-slip angle of 3° (nose-left). The reduced angle of attack on the fin, resulting from the side-slip angle, leads to a higher load on the Fenestron for torque compensation. Because of the knowledge gained in the investigation of the fast descent flight condition TOP36, a reduction of the strongly oscillating detachment around the tail boom is to be expected by the higher loading of the Fenestron and thus a defined flow through the Fenestron duct. An associated reduction of the structural dynamical excitation would correspond to the flight test classification of this flight state.

In order to keep the computational effort for this investigation within a manageable framework, a coarsened setup is used (Figure 27). Marginal geometric

Fig. 27: Surface of the coarse Bluecopter^{TM} CFD setup

simplifications (no rotor blade connections, simplified hub geometry, no Fenestron stator), as well as the negligence of the engine exhaust are applied. The resulting cell amount is 72 M cells and a temporal resolution of 1° main rotor azimuth is used. A 6-DoF flight mechanic trim is carried out. The resulting control and fuselage orientation angles deviate less than 0.5 ° from the ones measured in the flight test, only the pitch orientation is overestimated by 1.7 ° (nose up). This deviation indicates an airframe drag underestimation and, therefore, lower propulsion required due to neglected mounting parts and surface unevenness in the CFD.

In order to allow a comparison with the flight TOP36 and to prevent resolution effects, this is also calculated with the coarse setup. A damping of $\zeta = 0.08$ is applied compared to the fine resolution with $\zeta = 0.04$. This results from the poorer resolution of small-scale turbulence and the associated stronger excitation of the low-frequency mode shapes.

9.1 Tail boom vibrations

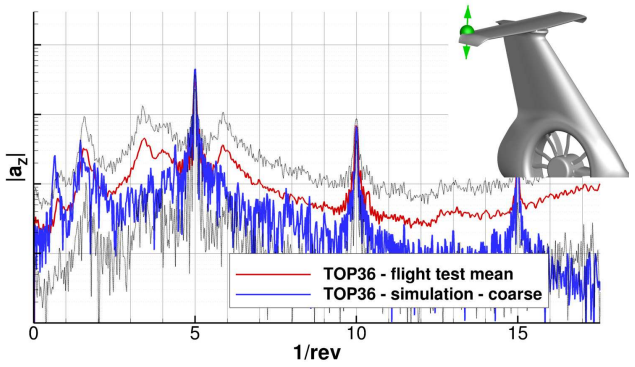

(a) TOP36 - slight tail shake

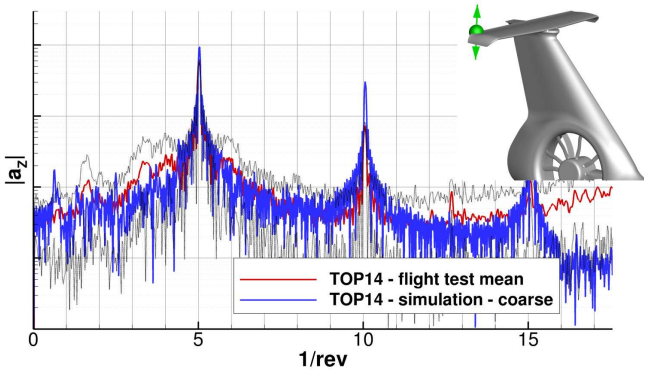

(b) TOP14 - minor tail shake

Fig. 28: Comparison of acceleration measurements at different flight states (grey indicates flight test variation)

Figure 28 shows the acceleration measurements of the two flights. In the case of TOP36 (cf. Figure 28 a)), the characteristics are also very well represented with the coarse resolution, whereas the broadband noise is significantly lower compared to the highly resolved calculation. The level flight TOP14 (cf. Figure 28 b)), which is classified as a minor tail shake case, shows a significantly lower excitation of the low-frequency vibrations. The first vertical bending mode is still present with a slightly distinctive amplitude, while the torsion modes disappear almost completely. This behavior is very well represented in the simulation. The changed flight situation results in a much stronger stimulus of the BPF harmonics. This is also represented in the simulation, with the location of the tip vortices closer to the horizontal stabilizer resulting in a stronger impulsive character of the acceleration. This coincides with the larger pitch angle, which is overestimated by the 6-DoF trim compared to the flight test.

The simulation with the coarse grid already shows that good agreement of the fundamental characteristics with the excitation of the striking frequencies can also be achieved with moderate resolutions of the CFD. However, in case of TOP36, a slight underestimation of the broadband excitation is observable.

9.2 Fenestron operation

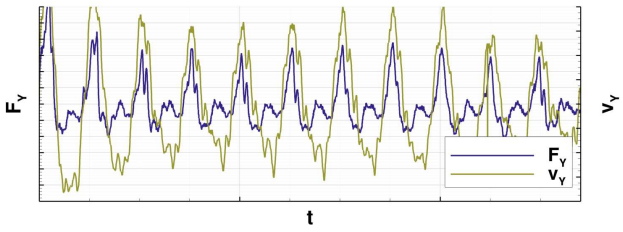

(a) TOP36 - rear Fenestron duct

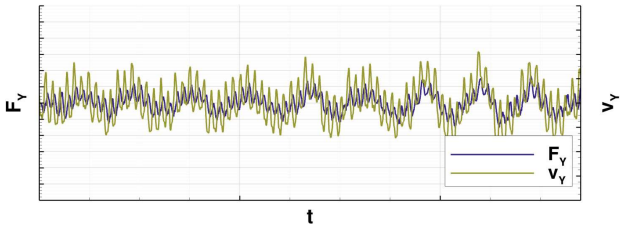

(b) TOP14 - rear Fenestron duct

Fig. 29: Lateral force and velocity at rear Fenestron duct for different flight states (common ordinate scale)

A prominent sign for the horizontal stimulation of the tail boom vibrations in the previous section was a strong interaction between an average reverse thrust with a strong thrust oscillation of the Fenestron and a resulting suction area at the Fenestron duct. Due to the higher anti-torques for TOP14 and the resultant mean Fenestron thrust, local lateral force and velocity at the Fenestron duct are compared between the flight states in Figure 29. In case of the coarse TOP36 calculation, a stronger load fluctuation is formed than in the case of the fine calculation, which is in-phase with the tail boom vibration velocity. As expected, less high-frequency components are pronounced compared to the fine calculations. In case of TOP14, a significantly lower lateral tail boom speed is present which results from the lower excitation of the lateral bending mode. In addition, the load fluctuation at the duct is significantly weaker and is dominated by the blade passing frequency. This concludes that a significant influence of the Fenestron load condition correlates with the excitation of the tail boom.

It should be noted, however, that this findings can not be readily transferred to other helicopter designs. In the case of a conventional tail rotor, this load oscillation at the duct of course dispenses and larger stabilizers, with end plates, for example, could cause other critical load conditions.

10 CONCLUSIONS

From the work presented in this paper, the following conclusions can be derived:

- A time-resolved coupling framework between CFD and CSD has been implemented into our simulation framework and successfully validated against flight test data, which allows a physical insight into aeroelastic phenomena on the helicopter airframe.
- Estimations of various influence factors on the structural dynamics have been taken into account, based on a couple of simplifications which have been made (no main rotor movements, no precession effects of the Fenestron, rigid body movement of the complete Fenestron)
- The consideration of tail shake requires large non-periodic time windows for evaluation due to stochastic load and displacement fluctuations.
- The presented numerical method resolve the excitation of low-frequency tail boom eigenmodes with good agreement compared to flight test data.
- Due to the weak tail shake of the considered helicopter, no distinct reason of tail shake can be determined, but candidates have been identified. Strong load fluctuations at the reverse operating Fenestron's duct indicate a possible cause.
- The robustness of the method against flight state changes could be shown. A good consistency of tail boom vibrations is found in a flight state with slight and minor tail shake.
- The use of URANS for the CFD simulation leads to a slight underestimation of broadband noise.
- Moderately resolved CFD simulations already show good agreement with flight test data, but with stronger deviations in broadband noise and slightly overestimated low frequency vibrations.

Further steps should focus on the application of the process chain to helicopters with strong tail shake. A simulation of various design configurations influencing the tail shake can assess the sensitivity of the tool chain to map vibrations change. This enables the evaluation of the potential of this tool chain for derisking and optimizing with regard to tail shake characteristics of new helicopter designs.

An extension of the methodology by considering the current neglects is conceivable as a further improvement of the tool chain. Nevertheless, fundamental improvements are neither to be expected nor necessary on the basis of the knowledge gained within this investigation.

ACKNOWLEDGMENTS

This work was performed within the federal research project LuFo V-2 (FKZ 20H1501).

The authors would like to thank Airbus Helicopters Deutschland GmbH (AHD) for the esteemed cooperation within this project and beyond, as well as providing us experimental data to enable this investigation. The authors gratefully acknowledge Oliver Dieterich (AHD) for his engagement and professional support during this project and Christopher Ciavarella (AHD) for creating the CSD model of the Bluecopter™. We would like to express our thanks to the Federal Ministry of Economics and Technology for providing us with the resources to realize this project. Furthermore, the investigation is based on the long-standing cooperation with the German Aerospace Center (DLR), which made their CFD code FLOWer available for advancements and research purposes, which we would like to thank for.

Further acknowledgment is made to the High Performance Computing Center (HLRS) in Stuttgart who provided us with support and service to perform the computations on their high performance computing system Hazelhen.

REFERENCES

[1] Strehlow, H., Teves, D., and Polz, G., "Applied helicopter aeroelastics : modelling and testing," Proceedings of the 22nd European Rotorcraft Forum, Brighton, UK, 1996.

[2] de Waard, P. and Trouve, M., "Tail Shake Vibration: Objective Comparison of Aerodynamic Configurations in a Subjective Environment," Proceedings of the American Helicopter Society, 55th Annual Forum, Montreal, Canada, May 1999.

[3] VDI-2057, "Human exposure to mechanical vibrations: Whole-body vibration," , September 2002.

[4] Mazzucchelli, C. and Wilson, F., "The Achievement of Aerodynamic Goals on the EH101 Project Through the Single Site Concept," 17th European Rotorcraft Forum, Berlin, Germany, 1991.

[5] Roesch, P. and Vuillet, A., "New Designs for Improved Aerodynamic Stability on Recent Aerospatiale Helicopters," Proceedings of the American Helicopter Society, 37th Annual Forum, New Orleans, Louisiana, May 1981.

[6] Cassier, A., Weneckers, R., and Pouradier, J.-M., "Aerodynamic Development of the Tiger Helicopter," Proceedings of the American Helicopter

Society, 50th Annual Forum, Washington, DC., 1994.

[7] Hansen, K., "Handling Qualities Design and Development of the CH-53E, UH-60A, and S-76," Royal Aeronautical Society International Conference on Helicopter Handling Qualities and Control, London, UK, 1988.

[8] Hassan, A., Thompson, T., Duque, E., and Melton, J., "Resolution of Tail Buffet Phenomenon for AH-64D Longbow Apace," Proceedings of the 53rd Annual Forum of the American Helicopter Society, Virginia Beach, VA, 1997.

[9] Hermans, C., Hakkaart, J., Panosetti, G., Preatoni, G., Mikulla, V., Chery, F., and Serr, C., "Overview Of The NH90 Wind Tunnel Test Activities And The Benefits To The Helicopter Development," Proceedings of the 53rd Annual Forum of the American Helicopter Society, Virginia Beach, VA, 1997.

[10] Huber, H. and Masue, T., "Flight Characteristics Desing and Development of the MBB/KHI BK 117 Helicopter," 7th European Rotorcraft Forum, Garmisch-Patenkirchen, Germany, 1981.

[11] Kampa, K., Enenkl, B., Polz, G., and Roth, G., "Aeromechanic Aspects in the Design of the EC135," Proceedings of the 23rd European Rotorcraft Forum, Dresden, 1997.

[12] Renaud, T., O'Brien, D., Smith, M., and Potsdam, M., "Evaluation of Isolated Fuselage and Rotor-Fuselage Interaction using CFD," Proceedings of the American Helicopter Society, 60th Annual Forum, Baltimore, MD, June 2004.

[13] Busch, E. R., Wurst, M. S., Keßler, M., and Krämer, E., *High Performance Computing in Science and Engineering 12*, Springer Verlag, 2012, Chapter Computational Aeroacoustics with Higher Order Methods, pp. 239–253.

[14] Kowarsch, U., Oehrle, C., Hollands, M., Keßler, M., and Krämer, E., *High Performance Computing in Science and Engineering 13*, Springer Verlag, 2013, Chapter Computation of Helicopter Phenomena Using a Higher Order Method, pp. 423–438.

[15] Stanger, C., Kutz, M. B., Kowarsch, U., Busch, E. R., Keßler, M., and Krämer, E., *High Performance Computing in Science and Engineering 14*, Springer Verlag, 2014, Chapter Enhancement and Applications of a Structural URANS Solver, pp. 433–446.

[16] Kranzinger, P. P., Kowarsch, U., Schuff, M., Keßler, M., and Krämer, E., *High Performance Computing in Science and Engineering 15*, Springer Verlag, 2015, Chapter Advances in Parallelization and High-fidelity Simulation of Helicopter Phenomena, pp. 479–494.

[17] Kowarsch, U., Hofmann, T., Keßler, M., and Krämer, E., *High Performance Computing in Science and Engineering 16*, Springer International Publishing, 2016, Chapter Adding Hybrid Mesh Capability to a CFD-Solver for Helicopter Flows, pp. 461–471.

[18] Reveles, N. D., Blades, E. L., Bern, N. A., and Smith, M. J., "Capability for Fully Integrated Aeroelastic Simulation of Complete Vertical Lift Configurations," 73rd American Helicopter Society Annual Forum, Fort Worth, TX, 2017.

[19] Bebesel, M., D'Alascio, A., Schneider, S., Guenther, S., Vogel, F., Wehle, C., and Schimke, D., "Bluecopter Demonstrator - An Approach to Eco-Efficient Helicopter Design," 41th European Rotorcraft Forum, Munich, 2015.

[20] Kroll, N., Eisfeld, B., and Bleeke, H., "The Navier-Stokes code FLOWer," *Notes on Numerical Fluid Mechanics*, Vol. 71, 1999, pp. 58–71.

[21] Wilcox, D., "Multiscale Model for Turbulent Flows," *AIAA Journal*, Vol. 26, No. 11, 1988, pp. 1311–1320.

[22] Jameson, A., "Time dependent calculations using multigrid, with applications to unsteady flows past airfoils and wings," AIAA 10th Computational Fluid Dynamics Conference, Honolulu, HI, 1991.

[23] Kowarsch, U., Keßler, M., and Krämer, E., "High Order CFD-Simulation of the Rotor-Fuselage Interaction," 39th European Rotorcraft Forum, Moscow, 2013.

[24] Kowarsch, U., Keßler, M., and Krämer, E., "CFD-Simulation of the Rotor Head Influence to the Rotor-Fuselage Interaction," 40th European Rotorcraft Forum, Southampton, 2014.

[25] Kowarsch, U., Lippert, D., Schneider, S., Keßler, M., and Krämer, E., "Aeroacoustic Simulation of an EC145T2 Rotor in descent flight," 71th American Helicopter Society Annual Forum, Virginia Beach, VA, 2015.

[26] Kowarsch, U., Öhrle, C., Keßler, M., and Krämer, E., "Aeroacoustic Simulation of a complete H145 Helicopter in descent flight," 41th European Rotorcraft Forum, Munich, 2015.

[27] Borges, R., Carmona, M., Costa, B., and Don, W. S., “An improved weighted essentially non-oscillatory scheme for hyperbolic conservation laws,” *Journal of Computational Physics*, Vol. 227, (6), 2008, pp. 3191 – 3211.

[28] Toro, E. F., *Riemann Solvers and Numerical Methods for Fluid Dynamics*, Springer Verlag, Berlin, 1997.

[29] Johnson, W., *CAMRAD II Comprehensive analytical model of rotorcraft aerodynamics and dynamics*, fourth edition, 2009.

[30] Newmark, N. M., “A Method of Computation for Structural Dynamics,” *Journal of the Engineering Mechanics Division*, Vol. 85, (3), 1959, pp. 67–94.

[31] Chen, S.-S., *Flow-induced vibration of circular cylindrical structures*, Springer Verlag, Berlin, 1987.

[32] Placzek, A., Sigrist, F.-F., and Hamdouni, A., “Numerical simulation of an oscillating cylinder in a cross-flow at low Reynolds number: Forced and free oscillations,” *Computers & Fluids*, Vol. 38, (1), 2009, pp. 80 – 100.

[33] Khalak, A. and Williamson, C., “Motions, forces and mode transitions in vortex-induced vibrations at low mass-damping,” *Journal of Fluids and Structures*, Vol. 13, (7), 1999, pp. 813 – 851.

[34] Kowarsch, U., Öhrle, C., Keßler, M., and Krämer, E., “Aeroacoustic Simulation of a complete H145 Helicopter in descent flight,” *Journal of the American Helicopter Society*, Vol. 61, (4), 2016, pp. 1–13.

[35] Grawunder, M., Reß, R., Breitsamter, C., and Adams, N. A., “Flow characteristics of a Helicopter fuselage including a rotation rotor head,” 29th Congress of International Council of the Aeronautical Sciences, St. Petersburg, Russia, 2014.